Solar survey at Pic du Midi: Calibrated data and improved images

Laurent Koechlin, Luc Dettwiller, Maurice Audejean, Maël Valais, Arturo López Ariste

A&A 631, A55 (2019)
https://doi.org/10.1051/0004-6361/201732504

Astronomy & Astrophysics

Solar survey at Pic du Midi: Calibrated data and improved images

Laurent Koechlin[1], Luc Dettwiller[2], Maurice Audejean[3], Maël Valais[1], and Arturo López Ariste[1]

[1] Institut de recherches en astrophysique et planétologie, Université de Toulouse, CNRS, CNES, UPS, 14 Avenue Edouard Belin, 31400 Toulouse, France
e-mail: laurent.koechlin@irap.omp.eu
[2] Lycée Blaise Pascal, 36 Avenue Carnot, 63037 Clermont-Ferrand Cedex, France
[3] Observateurs associés, Rue de la Cau, 65200 Bagnères de Bigorre, France

Received 20 December 2017 / Accepted 5 September 2019

ABSTRACT

Context. We carry out a solar survey with images of the photosphere, prominences, and corona at Pic du Midi observatory. This survey, named CLIMSO (for CLIchés Multiples du SOleil), is in the following spectral lines: Fe XIII corona (1.075 μm), Hα (656.3 nm), and He I (1.083 μm) prominences, and Hα and Ca II (393.4 nm) photosphere. All frames cover 1.3 times the diameter of the Sun with an angular resolution approaching one arcsecond. The frame rate is one per minute per channel (weather permitting) for the prominences and chromosphere, and one per hour for the Fe XIII corona. This survey started in 2007 for the disk and prominences and in 2015 for the corona. We have almost completed one solar cycle and hope to cover several more, keeping the same wavelengths or adding others.
Aims. We seek to make the CLIMSO images easier to use and more profitable for the scientific community.
Methods. At the beginning of the survey, the images that we sent to the CLIMSO database were not calibrated. We have implemented a photometric calibration for the present and future images, in order to provide "science-ready" data. The old images have been calibrated. We have also improved the contrast capabilities of our coronagraphs, which now provide images of the Fe XIII corona, in addition to previous spectral channels. We also implemented an autoguiding system based on a diffractive Fresnel array for precise positioning of the Sun behind coronagraphic masks.
Results. The data, including the images and films, are publicly available and downloadable through virtual observatories and dedicated websites (use "CLIMSO" and "IRAP" keywords to find them). For the Hα and Ca II channels we calibrate the data into physical units, independent of atmospheric or instrumental conditions; we provide solar maps of spectral radiances in W m^{-2} sr^{-1} nm^{-1}. The instrumental improvements and calibration process are presented in this paper.

Key words. surveys – methods: data analysis – Sun: general – Sun: corona

1. Introduction

Pic du Midi de Bigorre in the French Pyrenées is the observatory where Bernard Lyot invented coronagraphy and obtained remarkable images in the 1930s and 1940s; see for example Lyot (1930, 1945, 1950). Since then, Pic du Midi has regularly provided high quality solar and coronagraphic data.

In a Lyot coronagraph, the bright image of the solar photosphere is blocked by an occulting disk of same diameter in the focal plane. Furthermore, the light diffracted around the occulting disk, which would be too bright to allow for observations of the corona, is in turn blocked by a "Lyot stop" in a pupil plane. Such an optical setup associated with precise baffling allows for a high rejection factor of solar light in the surrounding field, defined as the "dynamic range" in this work, which reaches 10^6.

This ongoing survey aims to help the scientific community with solar studies by providing a large set of solar images and films with dense temporal sampling: 1 min between frames, and long span: several solar cycles. We have kept constant the observation conditions: frame rate, field, wavelengths, and bandpass, but that does not forbid improvements on the image quality, such as arcsecond angular resolution, and high contrast (high dynamic range) as shown in Figs. 1 and 2.

At present, five instruments contribute to the CLIMSO (CLIchés Multiples du SOleil or Christian Latouche IMageur SOlaire) solar survey: two coronagraphs, two solar telescopes (Dettwiller & Noens 2008), and an autoguider. The autoguider uses a diffractive Fresnel array as a focuser and provides images of the Sun to center the other instruments.

We have been carrying out this survey since 2007 thanks to the important contribution of the "Observateurs associés", the volunteer astronomers[1] who contribute in many ways, including instrumental and software development, financial support, and yearlong handling of image acquisition.

Five instruments are placed on a single equatorial mount:
- c_1: Hα coronagraph, $\oslash$ 20 cm, λ 656.3 nm, $\Delta\lambda$ 250 pm
- c_2: He I coronagraph, $\oslash$ 20 cm, λ 1.083 μm, $\Delta\lambda$ 250 pm
- c_2: Fe XIII channel λ 1.0747 μm, $\Delta\lambda$ 250 pm
- l_1: Hα telescope, $\oslash$ 15 cm, λ 656.3 nm, $\Delta\lambda$ 50 pm
- l_2: Ca II telescope, $\oslash$ 9 cm, λ 393.4 nm, $\Delta\lambda$ 250 pm
- Fresnel diffractive telescope that feeds the autoguider: $\oslash$ 6.2 cm, λ 632.8 nm, $\Delta\lambda$ 1 nm.

The four solar telescopes with their acquisition software were conceived and built in 2006 by J.-C. Noëns, L. Dettwiller, D. Romeuf, and subcontractors (Dettwiller & Noens 2008). Since then, these telescopes have been providing images and films on a regular basis to the CLIMSO database[2].

Among several upgrades, solar telescope l_1 now has high quality optics and a new Hα filter. We have improved the baffling

[1] www.climso.fr
[2] climso.irap.omp.eu/data/archives.html

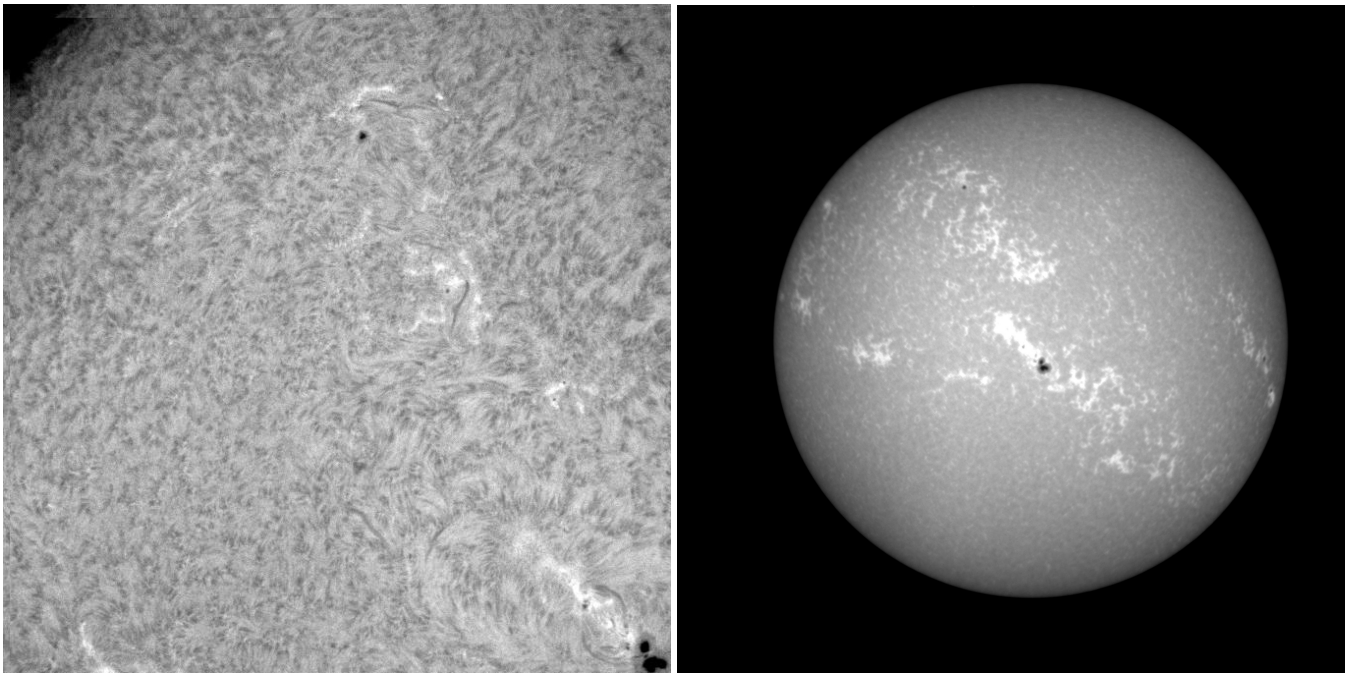

Fig. 1. *Left*: solar chromosphere in Hα at 656 nm. This cropped frame contains the top left quarter of the solar disk: approximately 810 × 810 arcsec; compare with the simultaneous image in Ca II on the right. The original image covers the full disk in 2k × 2k pixels. Images are taken every minute, from one hour after sunrise to one hour before sunset, weather allowing. *Right*: solar chromosphere in the Ca II line at 393.4 nm. These two images were taken with l_1 and l_2 at Pic du Midi (2015-03-27).

and especially the correction of the filter stack leakage in coronagraph c_2. In 2015 this led to the 10^6 dynamic range allowing for images of the solar corona.

We define the dynamic range of a coronagraph as the ratio between the brightness in the image of the photosphere and the residual light in the surrounding field at the final focal plane. This could also be called "rejection factor".

In good weather conditions, a set of four images is taken every minute, and one image of the solar corona in the Fe XIII line at 1074.7 nm is taken per hour. All images are uploaded to the database each night, along with several movies made from these images. During daytime, a few images are selected for real-time uploading to the data base.

2. Guiding system

The fifth telescope is used for guiding. The main optics of this telescope consist of a Fresnel diffractive array, 2.5 m in focal length at $\lambda = 633$ nm, placed close to the c_1 coronagraph. The coronagraph and diffractive optics for the guider are fastened to each other, thus limiting differential flexion.

The Fresnel diffractive array shown in Fig. 4 is a copper foil 80 μm thick and 65 mm in diameter with several thousand holes, based on the diffraction principle Fresnel (1818) and Soret (1875). This foil, or diffractive array, acts as a Fresnel zone plate and forms a sharp image of the Sun on a camera, which sends a frame or frames to an image processor. The diffractive Fresnel array has a binary transmission: 0 or 1 (Koechlin et al. 2005). There is no optical material in this objective lens, only opaque material (in this case, a thin copper plate: transmission 0) with holes of precisely calculated shapes (where transmission is 1) that focus light by constructive interference. This setup is lightweight, steady, affordable, and yields high contrast images.

This optical concept provides diffraction-limited images. It works with broadband (non-monochromatic) light as it can be corrected from chromatic aberration. Fresnel arrays have supplied high contrast images of sky objects; see Koechlin et al. (2012) and Koechlin (2014). Although these authors refer to tests with 20 × 20 cm square Fresnel arrays, these two publications provide references of studies for larger diffractive arrays.

Diffraction focusing causes chromatism in the resulting images at prime focus, but we do not need to cover this in this work: we placed a narrowband filter ($\lambda = 633$ nm, $\Delta\lambda = 1$ nm) near focus. This wavelength of He-Ne lasers does not correspond to a feature in the solar spectrum, so the images of the solar disk in the autoguider are prominence-free. This He-Ne filter is affordable; its spectral finesse (1 nm) is slightly too low for complete chromatism cancelation in this optical configuration, but the images are almost diffraction-limited.

To achieve a good contrast we had to block the light from unwanted diffraction orders; this mainly concerns order zero passing as a plane wave, unfocused through the Fresnel array. To block this order we used a central obscuration, casting its shadow on the focal plane. By geometric design, this also removes all positive and negative diffraction orders except the desired one. As the Sun is not a point source, the central obscuration (here 52 mm) needs to be larger than the required field for guiding. On the other hand, the outer diameter of the objective is limited by the size of the narrowest Fresnel rings in the diffractive array, which can be grooved and is itself limited by the waist of the UV laser beam used to manufacture it. The local machine tools that were used have a laser beam width of 20 μm, thus limiting the Fresnel array diameter to 62 mm for 2.5 m focal length at 633 nm. Recent machine tools with thinner laser beams can manufacture much wider Fresnel arrays with equal focal length.

An image of the Sun is taken every second by a SBIG-8300F camera at focus behind a small lens adapting the field scale to the camera sensor; this image is then sent to the autoguider software, which keeps the five instruments precisely pointed, even when

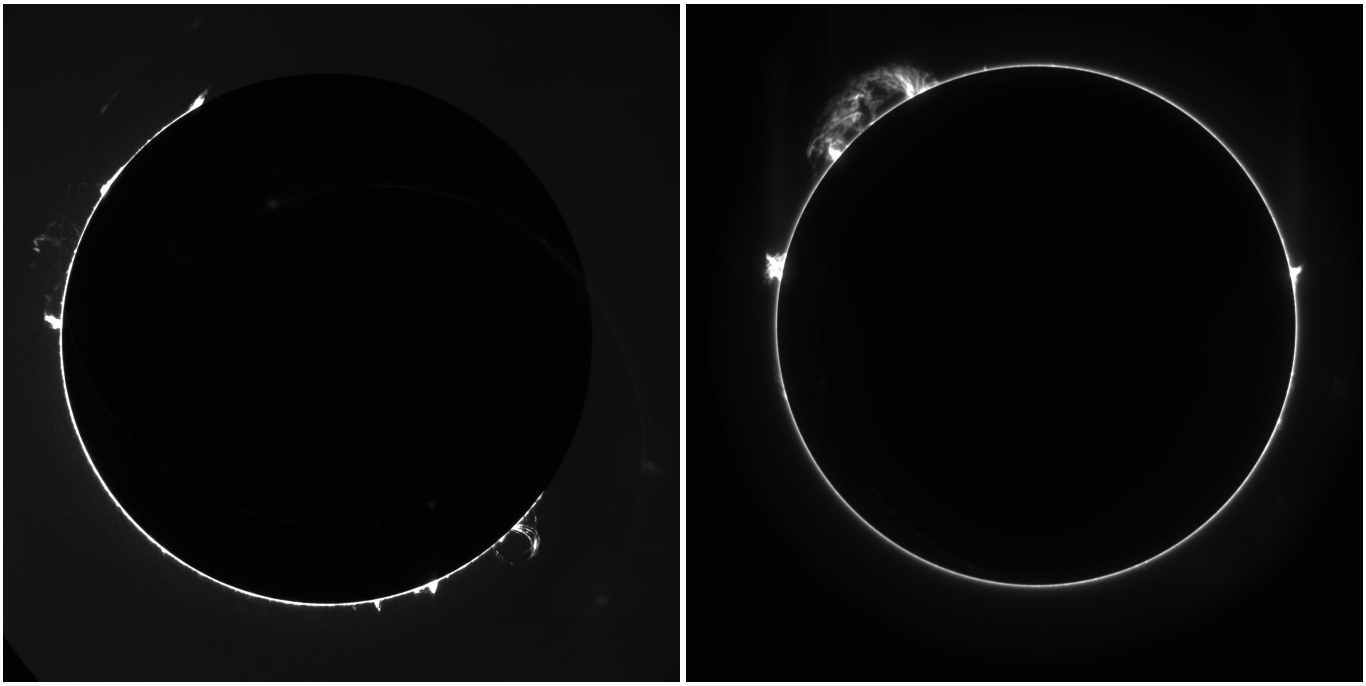

Fig. 2. *Left*: solar prominences in Hα at 656.28 nm, taken with c_1 during the solar eclipse of 2015-03-20. The dark lunar disk blocks the light in the top right part of the field. *Right*: solar prominences in the He I line at 1.0830 μm, taken with c_2, 2015-03-27.

the Sun disk is partly blocked by clouds or by the moon; see bottom of Fig. 4.

The solar disk is processed to extract its edge (ring or arc), which in turn is correlated with a reference circle. The guiding software adapts the diameter of that circle to the apparent diameter of the Sun. The position of the reference circle can be either manually or automatically adjusted to any desired position. To reduce the processing time we use sparse matrix algorithms rather than fast Fourier transforms. The computed distance between the center of the reference circle and the center of the solar disk is used to determine a command sent to the equatorial mount. The source code in C++ and a detailed documentation of the autoguider are available on github[3].

The guiding precision is better than 1 arcsec in good seeing conditions. Of course, because of the slow sampling rate of 1 s and the inertia of the equatorial mount, most of the tip-tilt agitation due to atmospheric seeing is not corrected. This limitation in performances is significant in bad seeing or high wind conditions. We plan to improve the algorithm that computes the commands to the equatorial mount based on the history of solar positions found; at present it is just a proportional response.

3. Photometric image calibration

3.1. Principle

Our photometric calibration is based on the fact that in an image of the Sun made from the ground, the sum of all pixels in the solar disk represents the total light received from the Sun through the spectral bandpass of the instrument. If we have an independent measure of the corresponding solar power above the atmosphere, such as a calibrated solar spectrum obtained by a space-borne system, and if we make the approximation that the solar absolute magnitude can be considered constant, we can deduce a calibration factor for any image made under the atmosphere. This calibration globally takes into account the atmospheric and instrumental transmission for that particular image.

3.2. Preprocessing

This calibration process concerns the past, present and future images of the ongoing survey. This process is applied to the images each day, just before the data are uploaded to the database.

In the first steps of this process, we correct the images from dark and flat-field effects induced by the cameras: charge-coupled device (CCD) on solar telescopes $l1$ and $l2$, and complementary metal oxide semiconductor (CMOS) on coronagraphs $c1$ and $c2$. As the exposure times are all very short, we considered that the bias and dark images are equivalent. The pixel scale is calibrated from the angular diameter of the Sun each time a modification is made to the optics. The rotation angles of the cameras and their variations during the day are also calibrated regularly, and the images are de-rotated so that the north solar pole is up.

We do not correct the geometrical distortion, but this error is very low: the optics in the coronagraphs and solar telescopes all have a long f-ratio and they work at small angles. For $l1$ and $l2$ we perform a photometric calibration explained in the following. The result is a spectral radiance map of the Sun.

At this point the cameras provide raw images of the solar disk that represent its local radiance, but these images are affected by (1) the Sun–Earth distance, (2) the absorption due to airmass and atmospheric conditions; and (3) the instrument, i.e., the optics transmission and camera response.

We calibrated those three parameters globally to obtain calibrated images that represent physical conditions at the surface of the Sun or its vicinity, so the pixel "brightness" values are in physical units. The choice of a relevant unit is not simple since the Hα, He I, Ca II K, and Fe XIII light forming the images is emitted

[3] https://github.com/maelvalais/climso-auto

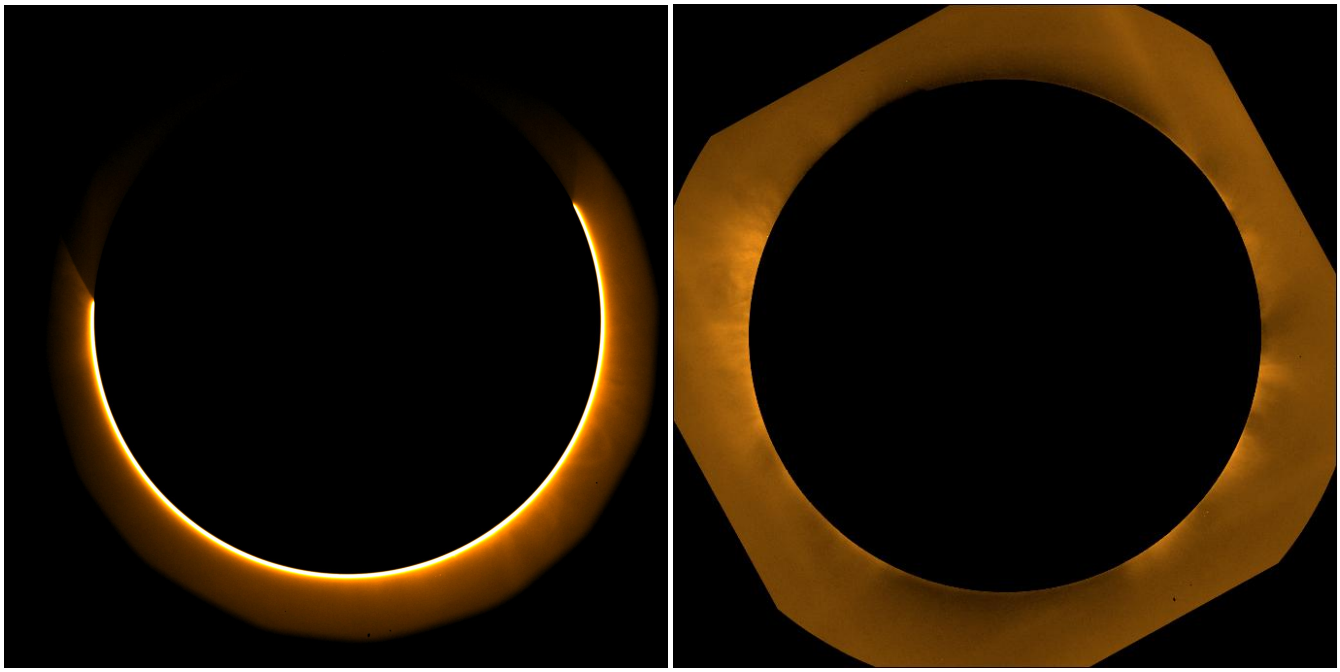

Fig. 3. *Left*: one of our first images of the Fe XIII corona at 1075 nm, taken with the *c*2 coronagraph (centered on the Sun) during a partial solar eclipse (2015-03-20). A coronal loop is clearly visible at 4 o'clock, and coronal jets on each side. The dark lunar disk (not centered on the Sun) blocks the upper left part of the solar ring and corona. At the two intersections, one can discern the circular shape of the Moon in front of the corona. *Right*: a more recent image of the solar corona at 1075 nm; a composite of 5 images taken with the *c*2 coronagraph between 07:39 and 07:57 on 2015-04-12, 6 s exposure time each. Images of the Fe XIII corona are now made on a regular basis at intervals of 30 min or 1 h every day, weather allowing.

from volumes of solar plasma (chromosphere, prominences, and corona) with various optical thicknesses and altitudes.

3.3. Photometric units

To make the following description of our calibration procedure as clear as possible, we introduce four photometric definitions that we use. They are described as follows.

In emission, (1) the radiance $L(x, y, \alpha, \delta)$, expressed in W m^{-2} sr^{-1}, is the flux emitted. This emission is in a given direction (α, δ), per unit of solid angle (sr), corresponding to the line of sight. This emission is from a point (x, y) of a surface, per unit area, (m^2) projected on a plane (the sky plane) normal to the considered direction (the line of sight). Also in emission, (2) the spectral radiance $L(x, y, \alpha, \delta, \lambda)$, expressed in W m^{-2} sr^{-1} nm^{-1}. We considered the emission toward the Earth, i.e., the emission quasi-perpendicular to an emissive surface (in the plane of the sky), but not necessarily parallel to the local solar surface. Thus we can express the spectral radiance in our direction (α, δ) as $L(x, y, \lambda)$.

In reception, (3) the illuminance $I(x, y)$ is the flux received from all directions, at a given point (x, y) of a collecting surface, per unit area. Also in reception, (4) the irradiance corresponds to the illuminance when the collecting surface is perpendicular to mean propagation, which is our case. The irradiance $I(x, y)$ is expressed in W m^{-2}, and the spectral irradiance $I(x, y, \lambda)$ is expressed in W m^{-2} nm^{-1}.

To link the radiance L emitted from a point S above the Sun to the irradiance L' received on Earth at P, we used Clausius' theorem found in Born & Wolf (1980), Klein (1970), written as

$$L' = TL, \tag{1}$$

where T is the transmission factor associated with the beam, when we neglect the effect of diffusion on the optical path, and assume the refraction index $n \simeq 1$ at S and P. For simplicity, when P is the image of S by an instrument, we used the same notation (x, y) for coordinates of S and P. As briefly explained in the first paragraph of this Sect. 3, we found a two-step approach to obtaining a radiance map of the Sun through the transmission of a telescope: first, the value of a pixel in a Lambertian situation is proportional to the radiance of the corresponding element of the Sun; second, the proportionality factor is uniform over the whole solar disk. Hence, the relative value of a pixel compared to the average all over the Sun is also the relative radiance, compared to the mean radiance of the whole Sun, which is known from airborne measurements.

3.4. Photometric calibration

To obtain a calibrated image of the solar disk, the physical data we want for a pixel is the radiance toward the Earth: $L(x, y)$ of the corresponding point on the solar disk, through the normalized transmission function of our filter $T(\lambda)$ (whose maximum is $T^{\max}$), plotted in Fig. 5, i.e.,

$$L(x, y) := \int_0^\infty \frac{T(\lambda)}{T^{\max}} L(x, y, \lambda) \mathrm{d}\lambda, \tag{2}$$

where $L(x, y, \lambda)$ is the local spectral radiance on the Sun; in a plane close to the surface of the Sun and perpendicular to the line of sight, as discussed in the last paragraph of Sect. 3.3 and in Sect. 3.2.

We made the following approximations:

(1) On the image plane we are in a Lambertian situation, close to the optical axis. (2) $T(\lambda)$ does not depend on (x, y), i.e., the filter is uniform in the field. (3) The instrument and camera defects are flat-fielded out, but in addition the atmospheric transmission is uniform over the image field. That is valid in clear sky

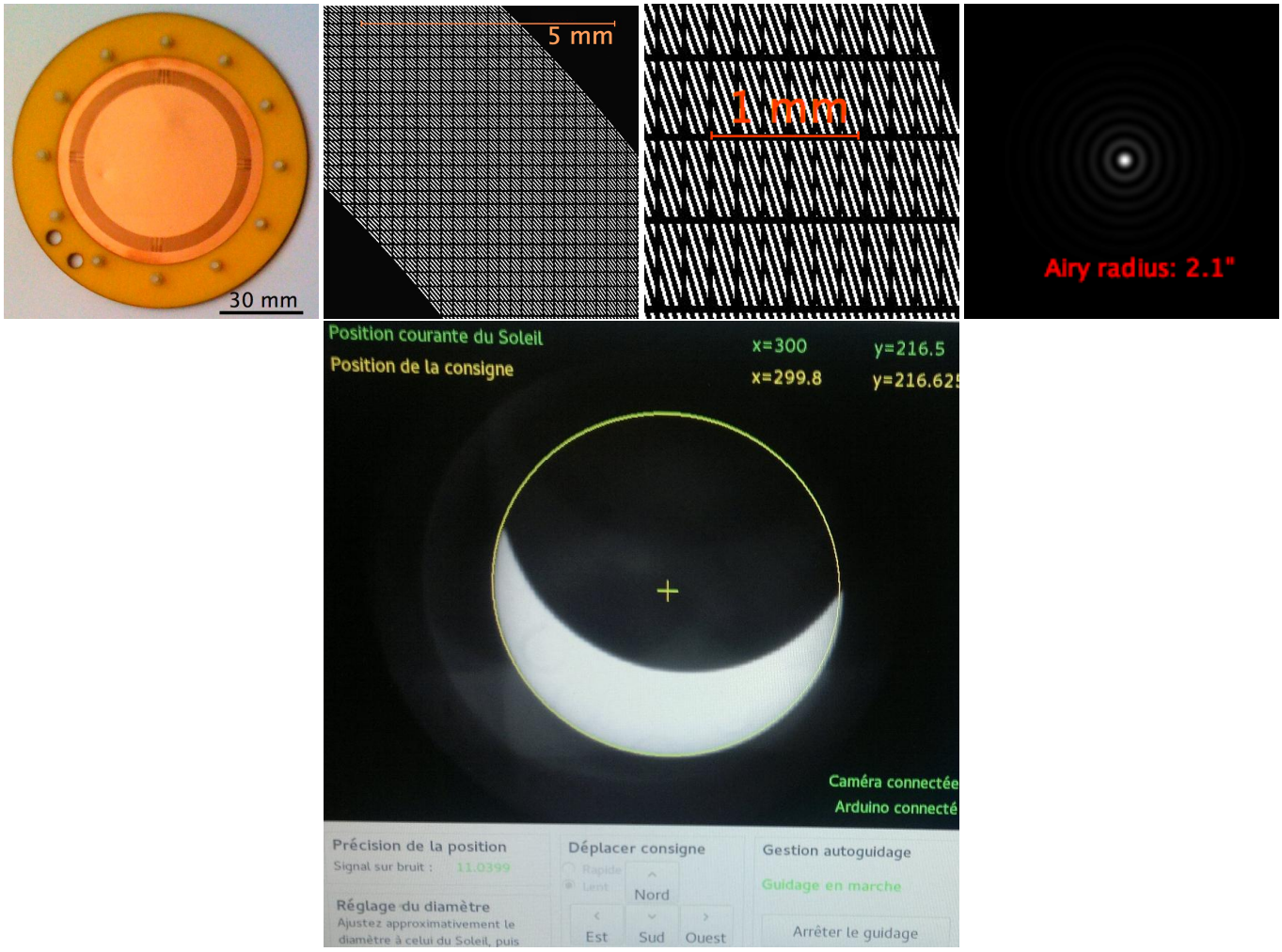

Fig. 4. Autoguider images. Its objective lens is a ring-shaped Fresnel array (*top left*): a thin copper plate with several thousand subapertures. An image of the Sun is formed by diffraction and interference through the holes. *Top center*: two enlarged views of the Fresnel array holes. *Top right*: image of a monochromatic point source (point spread function) given by the Fresnel array. *Bottom*: control screen (photo by Géraldine Pedezert) of the autoguider during the solar eclipse(2015-03-20). The solar disk is correctly located, even though only a crescent remains visible.

conditions and can be an approximation for a uniform haze or cirrus. (4) Our cameras have a linear and uniform response (once corrected from dark and flat-field); we assume that a raw pixel value $v(x, y)$, measured in arbitrary units *adu* for a point $P(x, y)$ in the image, is proportional to the local irradiance $L'(x, y)$ in that image.

The raw pixel value $v(x, y)$ is given by

$$v(x, y) \cong C \int_0^\infty T(\lambda) L(x, y, \lambda) \mathrm{d}\lambda. \quad (3)$$

- C is a transmission factor (constant over the image field, but variable in time) driven by the instrument, the Sun-Earth geometry, and the atmosphere, which is canceled out during the calibration process.
- The spectral transmissions of the atmosphere and optics, and the camera response contribute to C but they are slowly wavelength-dependent compared to the narrow filter bandpass $T(\lambda)$, so C can be considered wavelength independent in the relevant spectral band.

We take the variations of C with time, caused by changes of air mass or haziness, into account by the calibration process, as shown below. Changes in the instrument, such as aging of filters or cameras, which affect the global response, are also calibrated out by the same process. Furthermore, this will also be applied retrospectively to data that had not been calibrated when it was acquired. Care should be taken, however, that filter wavelengths are controlled and remain correct.

We know the equivalent bandpass $\Delta\lambda$ from the transmission function T, for l_1, is written as

$$\Delta\lambda := \int_0^\infty \frac{T(\lambda)}{T^{\max}} \mathrm{d}\lambda \cong (0.05 \pm 0.005)\,\mathrm{nm}. \quad (4)$$

The filter bandwidth and its precision are given by the manufacturer (Daystar).

We take, from the literature and documentation, the following data: a standard solar spectrum $I_{\lambda,\mathrm{m}}$ (averaged over a solar cycle), itself implicitly based on the solar constant, i.e., the standard solar irradiance at 1 AU; and spectral transmission of our filter $T(\lambda)$.

As we use narrowband filters, we need a calibrated standard solar spectrum at high spectral resolution. We start from an uncalibrated standard spectrum at high resolution: the Meudon Solar Atlas Delbouille et al.[4], then calibrate it with a calibrated

[4] http://bass2000.obspm.fr/solar-spect.php

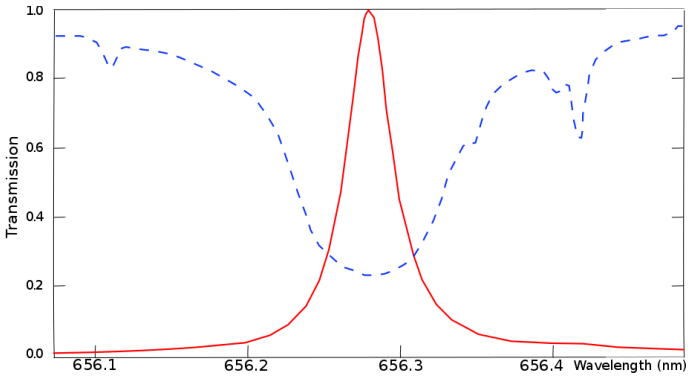

Fig. 5. Measurements by J.-M. Malherbe. Red curve: transmission profile of his $\Delta\lambda = 40$ pm bandwidth filter. For our calibrations we enlarged this profile to match the $\Delta\lambda = 50$ pm bandwidth profile of our filter from the same manufacturer (Daystar). We convolve the solar spectrum with this profile. The dotted line represents the central part of the Hα line in the solar spectrum, not normalized in this figure.

standard solar spectrum at lower resolution[5]: From that we compute I_m the standard solar irradiance above the Earth atmosphere integrated through the spectral profile of our filter, and we find its numerical value for l_1 (also in Table 1), i.e.,

$$I_m := \int_0^\infty \frac{T(\lambda)}{T^{max}} I_{\lambda,m}(\lambda) d\lambda \cong (0.018 \pm 0.001)\, W\, m^{-2}. \quad (5)$$

The ±0.001 error bar comes from the solar spectrum calibrations and the filter spectral curve: we have numerically integrated Eq. (5) to obtain the numerical value in W m^{-2}.

From this external data, and neglecting the cosine in the relation between the radiance and the elementary flux, we deduce for the current image L_m, the standard radiance averaged over the solar disk (D_m), and integrated through the transmission of the instrument,

$$L_m \cong I_m/\Omega_m \cong \int_{(D_m)} L\, d^2\Omega/\Omega_m, \quad (6)$$

where $\Omega_m \cong 0.680 \times 10^{-6}$ sr is the solid angle of the solar disk at 1 AU.

The ±5% uncertainty resulting from our estimation of I_m in Eq. (5) is much greater than the errors due to the effects of the cosine factor neglected in Eq. (6) and the distorsion. We now compare L_m with the average of the raw pixel values $v(x, y)$, over the N pixels covered by the solar disk image,

$$\sum_{j=1}^{N} \frac{v(x,y)}{N} := \bar{v}. \quad (7)$$

This average solar pixel value $\bar{v}$ corresponds to the apparent brightness of the solar disk through all the instrumental chain. From an independent source we have its calibrated brightness: L_m, calculated with Eq. (6), and we deduce the calibration factor C with

$$\bar{v} \cong C T^{max} L_m. \quad (8)$$

This allows us to eliminate C, and we finally find

$$L(x, y) \cong L_m\, v_r(x, y), \quad (9)$$

[5] rredc.nrel.gov/solar/spectra/am1.5/ASTMG173/ASTMG173.html

Table 1. Calibration factors.

Channel	Hα (l_1)	Ca II (l_2)
Central filter wavelength λ (nm)	656.28	393.37
Equiv. filter bandwidth $\Delta\lambda$ (nm)	0.050	0.25
$I_m(\lambda)$ above atm./W m^{-2} nm^{-1}	0.36 ± 0.02	0.33 ± 0.07
I_m integ. through filter/W m^{-2}	0.018	0.083
K solar surf./kW m^{-2} nm^{-1} sr^{-1}	529 ± 30	485 ± 90
L_m solar surf./kW m^{-2} sr^{-1}	26.5 ± 1.5	122 ± 26

Notes. First pair of lines: specifications of our filters. Middle: irradiance from the calibrated solar spectrum in blue from Fig. 6, integrated over the transmission curve. Bottom: calibration factors.

where $v_r(x, y) := v(x, y)/\bar{v}$ is the relative value of a pixel compared to the average, and

$$L(x, y) \cong K\, v_r(x, y), \quad (10)$$

where $K := L_m/\Delta\lambda$.

At present we calibrate the images similarly for our other solar telescope $l2$ in the Ca II line. We have a relatively inaccurate knowledge of the spectral transmission for the 10-year-old filter in telescope $l2$, in addition to the variability of the line, so we provide "calibrated" images with low precision. We plan to buy better filters in a few months.

The numerical values are listed in Table 1. In the third and fourth line of this table we have, corresponding to each filter, the mean spectral irradiance from the Sun above the Earth atmosphere, and then this spectral irradiance is integrated through the spectral curve specific to the filter. The calibration in Ca II is less precise because of the solar variability in that line, in addition to the aging of our Ca II filter. These are used to generate the calibrated images provided by the public database[6]. To keep a sufficient dynamic range in the 16 bit integer data, the pixel values in the database may be adjusted by a factor of 10. This will be documented in the Flexible Image Transport System (FITS) header. At present only the recent images have a calibrated counterpart, but all images since 2007 are going to be reprocessed and calibrated.

3.5. Future calibration of the Hα prominences

The spectral bandpass of the Hα filter in coronagraph c_1 is $\Delta\lambda_{c1} = 0.25$ nm. This can be considered to be wider than the emission lines of prominences, but narrow enough so that no significant emission from another phenomenon contributes to the pixel value $c_1(x, y)$ and

$$c_1(x, y) \cong C_{c1}\, T_{c1}^{max} L_{H\alpha}(x, y), \quad (11)$$

where $L_{H\alpha}(x, y)$ is the radiance at (x, y) over the Hα line of the prominences.

The images from coronagraph c_1 in the left panel of Fig. 2 cannot be calibrated similarly to l_2 and l_1 because it would require sampling the solar disk, which is too bright for c_1 and not adapted to its ring-shaped field. However, as c_1 and l_1 are centered on the same wavelength and both see the prominences (although c_1 is much more sensitive), a cross-calibration is possible. It is not simple to implement, but we propose the following approximations. First, the images on c_1 and l_1 can be considered

[6] http://climso.irap.omp.eu/data/index.html

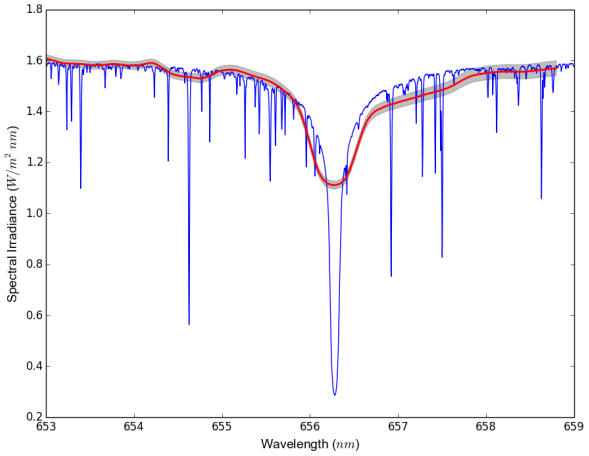

Fig. 6. Solar irradiance above the atmosphere in W m^{-2} nm^{-1} as a function of wavelength in nm. The blue curve is the FTS high resolution solar spectrum near Hα, Kurucz et al. (1984), which we use to calibrate the images taken with l_1 (λ = 656.28 nm; $\Delta\lambda$ = 50 pm). The red curve is shown for comparison. It is a calibrated solar spectrum taken at the ISS by Meftah et al. (2018). The gray zone around the red curve represents the area covered by its error bars. The wavelength axes of these two curves have been adjusted to each other. The superposition of the red and blue curves indicates a good agreement between data from the International Space Station and our calibration of the high resolution spectrum.

simultaneous as they are both taken within a few seconds interval. Second, the instrument characteristics and camera sensitivities evolve slowly and the average ratio between the responses of c_1 and l_1 can be considered constant for a few hours.

This image calibration for c_1 is not done yet, but is planned for the near future: we will use sets of prominences that have brightnesses within the linear response of both instruments l_1 and c_1: we find by least-squares fit the ratio Pro(l_1)/Pro(c_1) between images made by l_1 and images by c_1 of the same prominences.

As the radial velocities may drive some of the emission beyond the narrow bandpass of l_1 while still within the wider bandpass of c_1, special care will be taken in the algorithm to extract a precise brightness ratio from the histogram of ratios found.

3.6. Calibration for coronagraph c_2 is forthcoming

C_2 looks into the He I line at 1.0830 μm (Fig. 2, right; Fe XIII at 1.0747 μm, Fig. 3.) It cannot be calibrated yet as we have no solar photometer at that wavelength. We could compare the optics transmission and camera response at different wavelengths and then estimate a ratio for the air-mass effect, but this would be prone to many cumulative errors. For the moment and pending the implementation of a photometer in the corresponding waveband, for c_1 and c_2 we upload merely normalized images of prominences and corona.

4. Conclusions

We hope that our calibrated images contribute to the development of solar physics. We do not claim a high photometric precision immediately, but our calibrated images should be useful.

This calibration uses the solar spectrum, itself based on the solar constant; hence it can be done for any image, even if the image was obtained long ago, as long as it contains the solar disk (or a known fraction of this disk) with known wavelength and bandpass. To improve precision, we plan to reject spots, filaments, and eruptive regions when computing the solar disk average of each image. This CLIMSO database was started in 2007 and we hope to carry on for several solar cycles, and to complement other ground-based or space surveys. You are welcome to use it!

Acknowledgements. This set of instruments is operational all year long thanks to the 90 volunteer astronomers: the "Observateurs associés", who share the tasks of image acquisition, instrument development, and software with the staff at Observatoire Midi-Pyrénées (OMP) and Institut de recherche en astrophysique et planétologie (IRAP), in scientific collaboration with the "Programme national Soleil-Terre" (PNST). The Observateurs associés are funded by Fiducial (GEO Christian Latouche); IRAP and OMP are funded jointly by CNRS and Université de Toulouse. Special thanks to Raphaël Jimenez, Martine Lafon, Philippe Saby, Franck Vaissiére (president of the Observateurs associés), and the OMP staff, whose work has been crucial to the good operation of these instruments, computers, and networks. We thank the anonymous referee for his/her helpful comments.

References

Born, M., & Wolf, E. 1980, Principles of Optics – Electromagnetic Theory of Propagation Interference and Diffraction of Light (Pergamon: Oxford), 181
Dettwiller, L., & Noens, J.-C. 2008, Bull. Un. Prof. Phys. Chim, 102, 1227
Fresnel, A.-J. 1818, Mémoires de l'Académie des Sciences, 339
Klein, M. V. 1970, Optics (New York: Wiley), 121
Koechlin, L. 2014, in 40th COSPAR Scientific Assembly, COSPAR Meet., 40
Koechlin, L., Serre, D., & Duchon, P. 2005, A&A, 443, 709
Koechlin, L., Rivet, J.-P., Deba, P., et al. 2012, Exp. Astron., 33, 129
Kurucz, R. L., Furenlid, I., Brault, J., & Testerman, L. 1984, Solar Flux Atlas from 296 to 1300 nm (Sunspot, New Mexico: National Solar Observatory)
Lyot, B. 1930, Comptes rendus de l'Académie des Sciences, 191, 834
Lyot, B. 1945, ApJ, 101, 255
Lyot, B. 1950, Comptes rendus de l'Académie des Sciences, 231, 461
Meftah, M., Damé, L., Bolsée, D., et al. 2018, A&A, 611, A1
Soret, J.-L. 1875, Archives des Sciences physiques et naturelles, 52, 320